A Variational Approach for Pan-Sharpening

Faming Fang, *Student Member, IEEE*, Fang Li, Chaomin Shen, and Guixu Zhang

***Abstract*— Pan-sharpening is a process of acquiring a high resolution multispectral (MS) image by combining a low resolution MS image with a corresponding high resolution panchromatic (PAN) image. In this paper, we propose a new variational pan-sharpening method based on three basic assumptions: 1) the gradient of PAN image could be a linear combination of those of the pan-sharpened image bands; 2) the upsampled low resolution MS image could be a degraded form of the pan-sharpened image; and 3) the gradient in the spectrum direction of pan-sharpened image should be approximated to those of the upsampled low resolution MS image. An energy functional, whose minimizer is related to the best pan-sharpened result, is built based on these assumptions. We discuss the existence of minimizer of our energy and describe the numerical procedure based on the split Bregman algorithm. To verify the effectiveness of our method, we qualitatively and quantitatively compare it with some state-of-the-art schemes using QuickBird and IKONOS data. Particularly, we classify the existing quantitative measures into four categories and choose two representatives in each category for more reasonable quantitative evaluation. The results demonstrate the effectiveness and stability of our method in terms of the related evaluation benchmarks. Besides, the computation efficiency comparison with other variational methods also shows that our method is remarkable.**

***Index Terms*— Multi-spectral image (MS), panchromatic image (PAN), variational method, pan-sharpening, split Bregman, quantitative measures.**

I. Introduction

THE IMAGE data about the Earth acquired by satellites are very valuable in many areas, such as military intelligence, medical aid and disaster monitoring. However, satellites are expensive both in building and maintenance. This requires that we should do utmost to use the data obtained from the existing satellites. Many fine-resolution satellites, such as QuickBird and IKONOS, provide both multi-spectral (MS) and panchromatic (PAN) images, where MS image contains all spectral information of a region but has little spatial data, while PAN image only has high resolution spatial information. As an example, the IKONOS satellite provides four bands MS images with 4-m resolution and single band PAN images with 1-m resolution [1]. In order to use these data more effectively, the two types of images should be merged into a single image which contains more information, this merging process is called pan-sharpening or fusion.

The goal of pan-sharpening is to acquire a high resolution MS image by combining a low resolution MS image with a high resolution PAN image. The pan-sharpened result should be good enough to aid in various types of applications. As is well known, some tasks, such as contour extraction and pattern classification, require the high spatial data; others, e.g. target recognition and spectrum matching, desire the high spectral information. Therefore, the pan-sharpened image should have both high spectral and spatial qualities.

During the past few decades, various types of pan-sharpening methods have been presented [2], [3]. Many of them, such as the Intensity-Hue-Saturation (IHS) [4]–[6], Brovey [2], [7], Principal Component Analysis (PCA) [2], [4], Wavelet [8], [9] and Gram-Schmidt (GS) [10] methods, can be classified as component substitution methods (CS), where these methods are processed according to the following steps: up-sampling, alignment, forward transform, intensity matching, component substitution and reverse transform [11]. The common feature of the CS methods is that the fusion process is a tradeoff between the precise spectral quality and high spatial information. The pan-sharpened image is subjected to the spectral degradation while it has access to the high spatial quality. To acquire an image with both high spatial and spectral qualities, many advanced methods are presented recently (see [12], [13] for more details).

As a promising realm, variational method emerges recently. The main idea of the variational method is to build an energy functional based on some properties, and the minimum of the energy corresponds to the final result. Compared with other methods, the variational methods have many advantages in both theory and implementation [14]. More information about the variational method can be found in [14]–[16]. In 2006, based on the main assumption that the geometry of the MS bands should be contained in the topographic map of the PAN image, Ballester *et al*. [17] present the first variational pan-sharpening method named P+XS. The result of P+XS method is remarkable, but it suffers form some blurry. By combining the Wavelet and P+XS methods, Moeller *et al*. proposed a variational wavelet pan-sharpening method (VWP) [18], in which, they produce precise spectral information by using the wavelet term, and obtain clear spatial data through minimizing an energy term in P+XS. VWP can preserve spectral quality better while acquiring high spatial information. However, its result is still some room for improvement, and its time com-

Manuscript received September 19, 2012; revised March 19, 2013; accepted April 4, 2013. Date of publication April 16, 2013; date of current version May 22, 2013. This work was supported in part by the National Basic Research Program (973 Program) under Grant 2011CB707104, Program for New Century Excellent Talents in University under Grant NCET-08-0193, and the National Science Foundation of China under Grants 11001082 and 61273298. The associate editor coordinating the review of this manuscript and approving it for publication was Prof. Gang Hua. *(Corresponding author: G. Zhang.)*

F. Fang, C. Shen, and G. Zhang are with the Department of Computer Science, East China Normal University, Shanghai 201101, China (e-mail: fmfang@ecnu.cn; gxzhang@cs.ecnu.edu.cn; cmsheng@cs.ecnu.edu.cn).

F. Li is with the Department of Mathematics, East China Normal University, Shanghai 200241, China (e-mail: fli@math.ecnu.edu.cn).

Color versions of one or more of the figures in this paper are available online at http://ieeexplore.ieee.org.

Digital Object Identifier 10.1109/TIP.2013.2258355

plexity is much higher than those of many other algorithms. To reduce the complexity, the authors developed an alternate VWP (AVWP). Compared to VWP, AVWP requires less time, but it suffers more degradation in image quality.

Till now, due to the complexity of pan-sharpening, all of the existing methods are more or less deficient. Especially, in the variational pan-sharpening methods the assumptions might not be very perfect. This naturally leads us to consider some new assumptions from new perspectives, and to built a new model from them to obtain pan-sharpened images more accurately and effectively.

The key issue for pan-sharpening is to produce a pan-sharpened image which contains both high spectral and spatial qualities. In this paper, based on three basic assumptions, a new variational method is proposed to achieve this goal. Our main contributions are listed as follows:

- We propose three new assumptions, upon which an energy function is built.
- We discuss the existence of the minimizer of the proposed energy functional.
- We describe the numerical procedure for our energy based on the split Bregman framework.
- We divide the existing quantitative metrics into four categories, compare our method with others qualitatively and quantitatively, and discuss the efficiency of proposed method.

The rest of the paper is organized as follows. Section II presents three new assumptions and the corresponding energy functional for pan-sharpening. Section III analyzes the existence of the minimizer of the proposed energy. Section IV describes the numerical scheme to tackle the energy functional. Section V divides the existing quantitative metrics into four categories, and illustrates the experiments as well as the comparison studies. Finally, the paper is concluded in Section VI.

II. Proposed Method

In this section, we firstly present three new assumptions and the corresponding energy functional terms, then build the proposed total energy functional.

First of all, we introduce some notations that will be used later. Let $P : \Omega \to \mathbb{R}$ be a PAN image, $\boldsymbol{M} = (M_1, \ldots, M_N) : \Omega \to \mathbb{R}^N$ be an upsampled low-resolution MS image which has been upsampled to be the same size as P, and $\boldsymbol{u} = (u_1, \ldots, u_N) : \Omega \to \mathbb{R}^N$ be a high-resolution MS image (i.e., pan-sharpened image), where $\Omega \subset \mathbb{R}^2$ represents an open, bounded domain with Lipschitz boundary, and N is the number of bands of $\boldsymbol{M}$. For a random pixel $x \in \Omega$, $u_n(x)$ is the intensity of u_n at x, where $n \in \{1, \ldots, N\}$.

As aforementioned, we aim to obtain a pan-sharpened image from PAN and MS images. The pan-sharpened image should has both high spectral and spatial qualities to meet the requirements of various applications. Due to the nature of pan-sharpening, we can present three new assumptions as follows.

A. Assumption I: Spatial Information Preserving

As introduced in [19], spatial information of an image can be generally expressed by the measure of the gradient field. That is, given a PAN image P and a desired pan-sharpened band u_n, the spatial information can be represented by ∇P and ∇u_n.

Since in pan-sharpening, P contains most of the spatial information compared to $\boldsymbol{M}$, we shall assume that the linear combination among all bands of $\boldsymbol{u}$ could be close to P in spatial information. Mathematically

$$\sum_{n=1}^{N} \gamma_n \nabla u_n = \nabla P, \tag{1}$$

where γ_n represents the mixing coefficient which is nonnegative.

Some existing pan-sharpening methods, such as IHS [4]–[6] and P+XS [17], assume that

$$\sum_{n=1}^{N} \gamma_n u_n = P. \tag{2}$$

It is easy to find that (1) can be deduced from (2), but not vice versa. That is, our assumption (1) can be regarded as a generalization of assumption (2).

To impose our assumption into a variational framework, we present the following energy functional:

$$E_G(\boldsymbol{u}) = \int_\Omega \left| \sum_{n=1}^{N} \gamma_n \nabla u_n - \nabla P \right| dx. \tag{3}$$

B. Assumption II: Spectral Information Preserving

Generally, the pan-sharpened image $\boldsymbol{u}$ should appear clear and informative, while upsampled low-resolution MS image $\boldsymbol{M}$ is blurred and degraded. For this reason, $\boldsymbol{M}$ can be regarded as a degraded form of $\boldsymbol{u}$. That is, we can obtain $\boldsymbol{u}$ by enhancing $\boldsymbol{M}$.

Based on above analysis, we assume a local linear model between $\boldsymbol{u}$ and $\boldsymbol{M}$ for excellent enhance task, i.e., $\boldsymbol{M}$ is assumed as a linear transform of $\boldsymbol{u}$ in a size fixed neighborhood ω_x centered at the pixel x:

$$M_n(y) = a_n(x) u_n(y) + b_n(x) \quad \forall y \in \omega_x, x \in \Omega, \\ n = 1, \ldots, N, \tag{4}$$

where a_n and b_n are the linear coefficients which are constants in ω_x. This assumption have been proved reasonable in many areas such as image matting [20], dehazing [21], filter [22] and super resolution [23]. This local linear model ensures that $\boldsymbol{u}$ keeps the edge information of $\boldsymbol{M}$ since $\nabla M_n(y) = a_n(x) \nabla u_n(y)$, and enhances the boundary when $|a_n|$ is small.

To show the validity of this local linear model in remotely sensed images, we firstly acquire a sub-scene image from QuickBird satellite (size: 512×512, band: 4, data type: uint16, resolution: 2.8-m), then spatially degrade the image with low-pass filter and decimation operator by four to yield a 11.2-m resolution image. The 2.8-m and 11.2-m resolution images can be regarded as the pan-sharpened image $\boldsymbol{u}$ (see Fig. 1(a)) and low resolution MS image $\boldsymbol{M}$ (see Fig. 1(b)) respectively. This view is reasonable and has been used successfully in many literatures such as [24]. Obviously, an arbitrary local

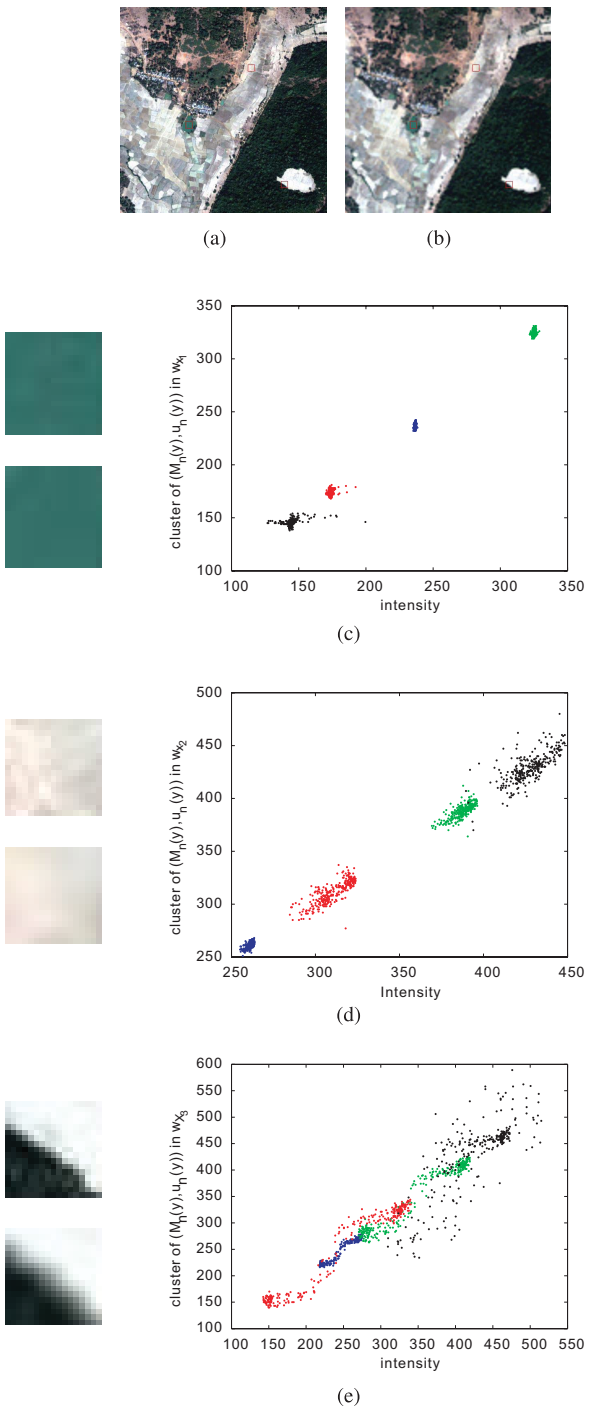

Fig. 1. Source QuickBird images and their points clusters. (a) The high-resolution MS images (RGB, 512×512 pixels). (b) The upsampled low-resolution MS image (RGB, 512×512 pixels). (c) Cluster of flatting area ω_{x_1} (RGB, 17×17 pixels): (1) top left: a flatting local area acquired from (a), (2) left bottom: the same local area acquired from (b), (3) right: the point cluster $\{(M_n(y), u_n(y)), y \in \omega_{x_1}\}$ for $n \in 1, \ldots, N$; blue, green, red, and black points are Clusters of 1, 2, 3, and 4 bands, respectively. (d) Cluster of smoothing area ω_{x_2} (RGB, 17×17 pixels), the meaning is similar to (c). (e) Cluster of jumping area ω_{x_3} (RGB, 17×17 pixels), the meaning is similar to (c).

area of an image can be classified as one of the three typical areas: flatting, smoothing and jumping areas. We thus select three typical areas, which are denoted by ω_{x_1} (flatting area), ω_{x_2} (smoothing area) and ω_{x_3} (jumping area), from the pan-sharpened image, and obtain the same areas in upsampled MS image. Then we construct point clusters $\{(M_n(y), u_n(y)), y \in \omega_{x_r}\}$ for all $n \in 1, \ldots, N$ and $r = 1, 2, 3$. The results are shown in Fig. 1(c)–(e) respectively. Observing on the figure, we find that although these clusters are not straight lines, their skeletons are roughly linear. That is, the local linear model is also valid in remotely sensed images.

Then, to impose this assumption into a variational framework, we present the following sums of the integral term:

$$E_S(\boldsymbol{u}, \boldsymbol{a}, \boldsymbol{b}) = \sum_{n=1}^{N} \int_{\Omega} \left\{ \int_{\omega_x} (a_n(x)u_n(y) + b_n(x) - M_n(y))^2 \, dy + \tau a_n^2(x) \right\} dx \quad (5)$$

where $\boldsymbol{a} = \{a_1, \ldots, a_N\}$, $\boldsymbol{b} = \{b_1, \ldots, b_N\}$, and τ is a controlling parameter keeping a_n away from been too large.

For the sake of computing convenience, we will rewrite formula (5). Firstly, we define a kernel,

$$k(x - y) = \begin{cases} \frac{1}{|\omega_x|}, & y \in \omega_x \\ 0, & \text{otherwise} \end{cases} \quad (6)$$

where $|\omega_x|$ is a constant. Obviously, $\int_{\Omega} k(x - y)dx = 1$.

Then we may rewrite (5) in form as

$$E'_S(\boldsymbol{u}, \boldsymbol{a}, \boldsymbol{b}) = \tau \sum_{n=1}^{N} \int_{\Omega} a_n^2(x) \, dx + \sum_{n=1}^{N} \int_{\Omega} \int_{\Omega} k(x - y) \times \left(a_n(x)u_n(y) + b_n(x) - M_n(y)\right)^2 dy \, dx. \quad (7)$$

Note that (5) and (7) differ by a constant multiple. We ignore it because it does not affect the energy.

C. Assumption III: Spectral Correction Preserving

The spectral signature of a MS image is important in many applications such as spectrum matching. Hence it is significant for preserving the spectral correlation information from the original low resolution MS image. To achieve this aim, we assume that the gradient in the spectrum direction of pan-sharpened image should be approximate to those of the original MS image, i.e.,

$$\nabla_s \boldsymbol{u} = \nabla_s \boldsymbol{M} \quad (8)$$

where $\nabla_s \cdot$ denotes the gradient in the spectrum direction.

Since an MS image only has N discrete bands, i.e., MS image is discrete in spectrum direction, the gradient $\nabla_s \boldsymbol{u}$ can be expressed as the following difference scheme,

$$\nabla_s \boldsymbol{u} = \{u_n - u_{n+1}, \ n = 1, \ldots, N - 1\}.$$

Therefore, (8) can be rewritten as:

$$u_n - u_{n+1} = M_n - M_{n+1}, \quad n = 1, \ldots, N - 1.$$

Obviously, the above equation is equivalent to

$$u_n - u_i = M_n - M_i, \quad i = n + 1, \ldots, N, n = 1, \ldots, N - 1.$$

Then we can impose this assumption into an energy form

$$E_C(\boldsymbol{u}) = \sum_{n=1}^{N-1} \sum_{i=n+1}^{N} \int_{\Omega} |u_n - u_i - M_n + M_i|^2 \, dx. \quad (9)$$

D. Energy Functional

Before building our energy functional, we need to define a functional space in which we search for a minimizer for $\boldsymbol{u}$. As introduced in [25]–[27], the space of functionals of bounded variation $BV(\Omega)$, i.e., $BV(\Omega) = \left\{u_n \in L^1(\Omega);\ \int_\Omega |Du_n| < \infty\right\}$, contains the set of piecewise smooth functions. It is a suitable space for images and has been frequently used in many image processing problems. Therefore, we choose $BV(\Omega)$ as our search space for u_n. Besides, we can select the space $L^2(\Omega)$ for a_n and b_n respectively.

Theoretically, in $BV(\Omega)$, ∇u_n may be undefined in some cases, whereas the distributional gradient Du_n is well-defined [16]. For this reason, we use Du_n instead of ∇u_n in what follows.

To fix our ideas, we propose obtaining the high-resolution MS image $\boldsymbol{u}$ by minimizing the total energy functional which is a combination of (3), (7) and (9), i.e.,

$$\begin{aligned} E(\boldsymbol{u},\boldsymbol{a},\boldsymbol{b}) &= E_G(\boldsymbol{u}) + \frac{\lambda}{2}E'_S(\boldsymbol{u},\boldsymbol{a},\boldsymbol{b}) + \frac{\nu}{2}E_C(\boldsymbol{u}) \\ &= \int_\Omega \left|\sum_{n=1}^N \gamma_n Du_n - DP\right| + \frac{\lambda\tau}{2}\sum_{n=1}^N \int_\Omega a_n^2(x)\,dx \\ &\quad + \frac{\lambda}{2}\sum_{n=1}^N \int_\Omega\int_\Omega k(x-y)\big(a_n(x)u_n(y) \\ &\quad + b_n(x) - M_n(y)\big)^2\,dy\,dx \\ &\quad + \frac{\nu}{2}\sum_{n=1}^{N-1}\sum_{i=n+1}^{N}\int_\Omega |u_n - u_i - M_n + M_i|^2\,dx \end{aligned} \tag{10}$$

where λ, ν are balancing factors adjusting the relations between E_G, E'_S and E_C, and the larger value indicates greater contribution of the corresponding term.

Let $\boldsymbol{BV}(\Omega) = \underbrace{BV(\Omega)\times BV(\Omega)\times\cdots\times BV(\Omega)}_{N}$, and the similar definition for $\boldsymbol{L}^2(\Omega)$. The total space Λ of our energy functional can be defined as

$$\Lambda = \{(\boldsymbol{u},\boldsymbol{a},\boldsymbol{b})|(\boldsymbol{u},\boldsymbol{a},\boldsymbol{b}) \in \boldsymbol{BV}\times\boldsymbol{L}^2(\Omega)\times\boldsymbol{L}^2(\Omega)\}. \tag{11}$$

After chosen the functional space, the minimum problem of our total energy functional (10) can be considered as the following regular form

$$\min_{(\boldsymbol{u},\boldsymbol{a},\boldsymbol{b})\in\Lambda} E(\boldsymbol{u},\boldsymbol{a},\boldsymbol{b}). \tag{12}$$

III. Existence of a Minimizer

In this section, the existence of a minimum for our energy will be proved based on the fundamental theorem of optimization. Firstly, we have to assume some assumptions on $\boldsymbol{a}$, $\boldsymbol{b}$, $\boldsymbol{u}$.

Assumption 1. *$|a_n(x)| \geq \varepsilon$, $|b_n(x)| \leq \mathcal{M}$, where $\varepsilon, \mathcal{M}$ denote universal strictly positive constants, and $n = 1,\ldots,N$.*

Remark 1. *As mentioned in Section II-B, u_n and M_n are linear related in a local area of x, where $a_n(x)$ and $b_n(x)$ are linear coefficients. Since M_n and u_n describe the same scene, they are highly related. Thus, we reasonably let $a_n(x)$ be larger than a certain but small value to prevent the degradation of linear relationship. For the same reason, $|b_n(x)| \leq \mathcal{M}$ is justified. Based on above analysis, Assumption 1 makes sense.*

Assumption 2. *$u_n \in BV(\Omega)$ meets: $\int_\Omega \big|\sum_{i=1}^N \gamma_i Du_i\big| \geq c\int_\Omega |Du_n|$ for some proper positive constant c.*

Remark 2. *From Assumption I in subsection II-A, we have $\sum_{n=1}^N \gamma_n \nabla u_n = \nabla P$. Since P contains more abundant spatial information than u_n, we have*

$$\int_\Omega |\nabla u_n| \leq \int_\Omega |\nabla P| = \int_\Omega \left|\sum_{i=1}^N \gamma_i \nabla u_i\right|.$$

Then Assumption 1 makes sense for some proper positive constant c.

Lemma 1. *The kernel k defined in (6) is bounded in $L^2(\Omega)$.*

Proof. Using the definition of k, the correctness of the lemma 1 can be easily verified by following reasoning,

$$||k||_2 = \int_\Omega \frac{1}{|\omega_x|^2}\,dx = \frac{1}{|\omega_x|^2}\int_\Omega dx = \frac{1}{|\omega_x|} < \mathcal{M}.$$

Considering the energy functional (12), we have the following theorem.

Theorem 1. *If $P \in BV(\Omega)$ and $\boldsymbol{M} \in \boldsymbol{L}^2(\Omega)$ are constants, under the assumptions 1 and 2, the minimization problem (12) admits a solution $(\boldsymbol{u}^*, \boldsymbol{a}^*, \boldsymbol{b}^*) \in \Lambda$.*

Proof. See Appendix.

IV. Numerical Schemes

In this section, the numerical procedure of the proposed energy (12) will be implemented. Since Du_n is usually treated as ∇u_n in difference scheme, we use ∇u_n instead of Du_n in the following numerical schemes.

As is well known, minimizing the energy (12) is equivalent to solving the Euler-Lagrange equation of (10). We thus calculate the first variations of functional (10) as

$$\frac{\delta E}{\delta a_n} = \lambda(\tau a_n + a_n k * u_n^2 + b_n k * u_n - k * (M_n u_n)) = 0 \tag{13}$$

$$\frac{\delta E}{\delta b_n} = \lambda(b_n + a_n k * u_n - k * M_n) = 0 \tag{14}$$

$$\begin{aligned} \frac{\delta E}{\delta u_n} &= -\gamma_n \mathrm{div}\left(\frac{\sum_{i=1}^N \gamma_i \nabla u_i - \nabla P}{|\sum_{i=1}^N \gamma_i \nabla u_i - \nabla P|}\right) \\ &\quad + \lambda(u_n k * a_n^2 + k * (a_n b_n) - M_n k * a_n) \\ &\quad + \nu\sum_{i=n+1}^{N}(u_n - u_i - M_n + M_i) = 0 \end{aligned} \tag{15}$$

where '*' denotes the convolution operation.

Given u_n, we can obtain the closed form solution of a_n and b_n from (13) and (14), which are shown as follows

$$a_n = \frac{k * [M_n u_n] - k * M_n \cdot k * u_n}{k * u_n^2 - [k * u_n]^2 + \tau} \tag{16}$$

$$b_n = k * M_n - a_n k * u_n. \tag{17}$$

Obviously, the solution of u_n can not be found directly. A classic method solving this problem is the gradient descent

method (GDM). However, because of the non-differentiability of the L^1 norm, a small positive parameter is added in GDM, which may lead to the inexact result. To overcome this drawback, many techniques, such as Chambolle's algorithm [28], augmented Lagrangian method [29] and split Bregman iteration [30], have been developed. Here we use the split Bregman iteration to solve our model.

A. Numerical Algorithm Based on Split Bregman Framework

We will now apply the split Bregman framework [30] to implement our minimization problem (12). As the closed form solution of a_n and b_n are given in (16) and (17), we only consider the sub-problem with respect to u_n.

As introduced in [30], the split Bregman iteration extends the utility of the Bregman iteration and linear Bregman iteration. It is a promising method which can solve the L^1 norm minimization problems effectively and can reduce the time and space overhead significantly.

The main idea of the split Bregman iteration is that it will separate the $l1$ and $l2$ components. Rather than considering (12), we present the following equivalent constrained problem

$$\min_{u_n,\boldsymbol{d}} \int |\boldsymbol{d}|\, dx + \frac{\lambda}{2}E'_S(\boldsymbol{u},\boldsymbol{a},\boldsymbol{b}) + \frac{\nu}{2}E_C(\boldsymbol{u}),$$
$$\text{s. t. } \boldsymbol{d} = \sum_{i=1}^{N}\gamma_i\nabla u_i - \nabla P.$$

To solve this problem, we firstly convert it to an unconstrained problem using the efficient Bregman iteration approach [30]

$$\begin{aligned}(u_n^{j+1},\boldsymbol{d}^{j+1}) = \arg\min_{u_n,\boldsymbol{d}} &\int_\Omega |\boldsymbol{d}| \\ &+\frac{\mu}{2}|\boldsymbol{d} - \sum_{i=1}^{N}\gamma_i\nabla u_i + \nabla P - \boldsymbol{e}^j|^2\, dx \\ &+\frac{\lambda}{2}E'_S(\boldsymbol{u},\boldsymbol{a},\boldsymbol{b}) + \frac{\nu}{2}E_C(\boldsymbol{u}) \qquad (18)\end{aligned}$$

$$\boldsymbol{e}^{j+1} = \boldsymbol{e}^j - \boldsymbol{d}^{j+1} + \sum_{i=1}^{N}\gamma_i\nabla u_i^{j+1} - \nabla P. \qquad (19)$$

In order to solve (18), we shall perform this minimization efficiently by alternate iteration with u_n and $\boldsymbol{d}$ separately. The two steps are performed as

$$\begin{aligned}u_n^{j+1} = \arg\min_{u_n} &\frac{\mu}{2}\int_\Omega \left|\boldsymbol{d}^j - \sum_{i=1}^{N}\gamma_i\nabla u_i + \nabla P - \boldsymbol{e}^j\right|^2 dx \\ &+ \frac{\lambda}{2}E'_S(\boldsymbol{u},\boldsymbol{a},\boldsymbol{b}) + \frac{\nu}{2}E_C(\boldsymbol{u}) \qquad (20)\end{aligned}$$

$$\begin{aligned}\boldsymbol{d}^{j+1} = \arg\min_{\boldsymbol{d}} &\int_\Omega |\boldsymbol{d}| \\ &+ \frac{\mu}{2}\left|\boldsymbol{d} - \sum_{i=1}^{N}\gamma_i\nabla u_i^{j+1} + \nabla P - \boldsymbol{e}^j\right|^2 dx. \qquad (21)\end{aligned}$$

Because the subproblem (20) is differentiable, optimality conditions for u_n^{j+1} are easily obtained. By differentiating with respect to u_n, we can derive that

$$Ku_n^{j+1} = rhs \qquad (22)$$

where

$$\begin{aligned}K &= -\mu\gamma_n^2\Delta + \lambda k * (a_n^j)^2 + \nu(N-n), \\ rhs &= -\mu\gamma_n \mathrm{div}\left(\boldsymbol{d}^j - \sum_{i=1,i\neq n}^{N}\gamma_i\nabla u_i^j + \nabla P - \boldsymbol{e}^j\right) \\ &\quad - \lambda(k*(a_n^j b_n^j) - M_n k * a_n^j) + \nu\sum_{i=n+1}^{N}(u_i + M_n - M_i)\end{aligned}$$

and Δ denotes the Laplacian operator.

Obviously, (22) is equivalent to

$$\mathcal{F}(K)\mathcal{F}(u_n^{j+1}) = \mathcal{F}(rhs) \qquad (23)$$

where $\mathcal{F}$ denotes the Fast Fourier Transform (FFT).

As solving the above equation for $\mathcal{F}(u_n^{j+1})$, we take $\mathcal{F}^{-1}$, the inverse FFT, to obtain the closed form solution of u_n^{i+1}, i.e.,

$$u_n^{j+1} = \mathcal{F}^{-1}\left(\frac{\mathcal{F}(rhs)}{\mathcal{F}(K)}\right). \qquad (24)$$

The solution of subproblem (21) can be given directly by the following the soft-thresholding formula

$$\boldsymbol{d}^{j+1} = \mathrm{shrink}\left(\sum_{i=1}^{N}\gamma_i\nabla u_i^{j+1} - \nabla P + \boldsymbol{e}^j, \frac{1}{\mu}\right), \qquad (25)$$

where

$$\mathrm{shrink}(x,\varsigma) = \frac{x}{|x|}\cdot\max(|x|-\varsigma, 0). \qquad (26)$$

Taking all above into account, the iteration with respect to subproblem u_n is summarized as follows:

$$\begin{cases} u_n^{j+1} = \mathcal{F}^{-1}\left(\frac{\mathcal{F}(rhs)}{\mathcal{F}(K)}\right) \\ \boldsymbol{d}^{j+1} = \mathrm{shrink}(\sum_{n=1}^{N}\gamma_n\nabla u_n^{j+1} - \nabla P + \boldsymbol{e}^j, \frac{1}{\mu}) \\ \boldsymbol{e}^{j+1} = \boldsymbol{e}^j - \boldsymbol{d}^{j+1} + \sum_{n=1}^{N}\gamma_n\nabla u_n^{j+1} - \nabla P. \end{cases} \qquad (27)$$

The steady state of the iteration is reached when the relative error between two iterates is less than 10^{-3} for all bands, i.e.,

$$\max_{n=1,\ldots,N}\left(\frac{||u_n^{j+1} - u_n^j||}{||u_n^j||}\right) < 10^{-3}.$$

Using above solvers, and taking the assumptions 1 and 2 into account, the overall procedure of proposed method can be shown in Algorithm 1.

In Algorithm 1, it should be noted that the constraints of a_n and b_n (provided by the Assumption 1) are shown in the first two equations, while the constraint of u_n (provided by the Assumption 2) is given in the last equation. Extensive experiments based on real data demonstrate that, provided that the positive constants c, ε are sufficiently small and $\mathcal{M}$ is adequately large, i.e., $c, \varepsilon \leq 10^{-16}$ and $\mathcal{M} \geq 10^{16}$, the perturbation of a_n caused by the constraint is negligible small, and b_n and u_n meet the constraints all the time.

Algorithm 1 The Overall Procedure for Proposed Model

Input: the low-resolution MS image $\boldsymbol{M}$ and the high-resolution PAN image P

Initialize: $\boldsymbol{u} = \boldsymbol{M}$, and $\boldsymbol{d}^0 = \boldsymbol{e}^0 = \mathbf{0}$. Fixed μ, τ, λ and ν

while $\max_{n=1,..,N} \left(\frac{||u_n^{j+1} - u_n^j||}{||u_n^j||} \right) \geq 10^{-3}$

  for $n = 1, .., N$

$a_n^j = \max(\frac{k*[M_n u_n^j] - k*M_n \cdot k*u_n^j}{k*(u_n^j)^2 - [k*u_n^j]^2 + \tau},\ \varepsilon)$

$b_n^j = \min(k * M_n - a_n^j k * u_n^j,\ \mathcal{M})$

$u_n^{j+1} = \mathcal{F}^{-1}\left(\frac{\mathcal{F}(rhs)}{\mathcal{F}(K)}\right)$

$\boldsymbol{d}^{j+1} = \text{shrink}(\sum_{n=1}^N \gamma_n \nabla u_n^{j+1} - \nabla P + \boldsymbol{e}^j, \frac{1}{\mu})$

$\boldsymbol{e}^{j+1} = \boldsymbol{e}^j - \boldsymbol{d}^{j+1} + \sum_{n=1}^N \gamma_n \nabla u_n^{j+1} - \nabla P$

restrict u_n^{j+1}: $u_n^{j+1} = u_n^{j+1} \cdot \min(1, \frac{\| \sum_{i=1}^N \gamma_i \nabla u_i^j \|}{c \| \nabla u_n^j \|})$

  end

end

Output: the pan-sharpened image $\boldsymbol{u}$.

V. Experimental Results and Analysis

In this section, in order to examine the effectiveness of proposed fusion method, we describe and analyze the experimental results on the QuikBird-2 and IKONOS-2 satellites data. The QuickBird-2 is a fine resolution satellite which provides MS images at 2.44-2.88 m resolution and PAN images at 0.61–0.72 m resolution [31], while the IKONOS-2 satellite captures 4-m MS images and 1-m PAN images [32]. The MS image of the both satellites contain four bands ($N = 4$), i.e., blue, green, red and near-infrared bands. Particularly, a detailed introduction of the satellite images can be found in [1].

We note that all the following experiments are implemented in MATLAB 7.12 and run on an Intel(R) 2.33 GHz machine with 4 GB RAM. Unless otherwise specified, we set $\gamma_n = 0.25$ in the following experiments, and one may choose a different value based on the different applications (see [33]). The radius of the ω_x (denote as R) and τ are set according to the analysis of [22], i.e., $R = 16$ and $\tau = 0.08^2$. We have found that our algorithm is insensitive to λ, ν and μ due to its stability [30], and $\lambda, \nu \in [0.01\ 0.5]$, $\mu \in [0.2\ 1]$ are acceptable.

A. Evaluation Metrics for Image Fusion

To evaluate different fusion methods, we need to consider the all-sided property of fusion tasks. However, the evaluation of image fusion is a foundational and challenging work so far [40]. The existing evaluation techniques can be roughly divided into two categories: qualitative analysis methods and quantitative analysis methods [41], where qualitative methods analyze the pan-sharpened result using human visual system (HVS) directly, while quantitative methods assess the fused image by using some quantitative metrics. Obviously, qualitative methods are relatively straightforward but difficult to implement due to the instability of the HVS. Quantitative methods are more objective and stable, but it requires an universal recognized criteria. Since no universal standard has been performed, quantitative methods can not be used as the only trustworthy method for evaluation. As this reason, the qualitative and quantitative analysis are both considered in this paper.

Many techniques have been proposed for quantitative analysis [7], [35], [36], [42]. Based on the different aspects they tend to, we may divided their methods into four categories:

- **Spectral quality metrics** Spectral quality metrics evaluate the quality of the fusion result by the preserving degree of the spectral informations, i.e., the level of change from $\boldsymbol{M}$ to $\boldsymbol{u}$. A smaller change indicates a better fusion work. This metrics include root mean squared error (RMSE) [7], [34], relative dimensionless global error in synthesis (RDGES) [33], relative average spectral error (RASE) [43] and objective quality fusion measure (Q_W) [19], [44]–[46], etc.
- **Spectral correlation quality metrics**
  Their metrics indicate the preserving degree of the spectral correlation information through the fusion process. For an outstanding fusion task, the correlation value between bands of $\boldsymbol{u}$ should be close to that of $\boldsymbol{M}$. There are many methods belong to spectral correlation quality metrics, such as correlation coefficient (CC) [35], [36], universal image quality index (UIQI) [18], [47], spectral angle mapper (SAM) [12], [24] and spectral information divergence (SID) [48].
- **Spatial quality metrics**
  Spatial quality metrics record the distortion degree of the spatial information. Since the spatial information is mainly contained in P, we only need to compare the fused image $\boldsymbol{u}$ with P. The spatial information of $\boldsymbol{u}$ should be equivalent to that of P in an ideal fusion work. Filtered correlation coefficient (FCC) [8], [18] and objective image fusion performance measure (Q^F) [37] are two examples of this metrics.
- **Image quality metrics**
  Image quality metrics evaluate the fusion by using the fused image $\boldsymbol{u}$ only. Its main idea is that a better fusion task should produce an image that has more details and informations. This metrics contain many methods, for example average gradient (AG) [39], spatial frequency (SF) [38] and entropy (H) [39].

Since each category of metrics has its own focus, and is not all-sided, a basic idea is that we take all categories of the metrics into account for a comprehensive evaluation. Due to space limitations, in this paper, we consider two typical evaluation methods for each category. These metrics are shown in Table I.

B. Qualitative Visual Analysis

Large number of fusion methods have been performed, and many of them have achieved promising results. We now visually compare our method with six popular pan-sharpening methods, namely, the standard IHS method (SIHS) [4], the adaptive IHS method (AIHS) [5], the wavelet method [8], [49], the P+XS method [17], the variational wavelet pan-sharpening method (VWP) [18] and the alternate VWP method (AVWP) [18]. We note that all parameters of

TABLE I
EIGHT METRICS AND THESE DEFINITIONS

Category	Metric	Definition	References Value	Meaning
Spectral quality metrics	RMSE [7], [34]	$\mathrm{RMSE} = \sqrt{\frac{1}{N\lvert\Omega\rvert}\sum_{n=1}^{N}\int_{\Omega}(u_n - M_n)^2\,dx}$.	0	The smaller the better.
	RDGES [33]	$\mathrm{RDGES} = 100r\sqrt{\frac{1}{N}\sum_{n=1}^{N}\left(\frac{RMSE(u_n,M_n)}{\overline{u}_n}\right)}$, where r is the ratio between the size of P and M_n, and $\overline{u}_n$ is the mean of u_n.	0	
Spectral correlation quality metrics	CC [35], [36]	$\mathrm{CC} = \frac{2}{N(N-1)}\sum_{n=1}^{N}\sum_{m=1}^{n}\lvert Cor(M_n,M_m) - Cor(u_n,u_m)\rvert$ where $Cor(M_n,M_m) = \frac{\int_{\Omega}(M_n-\overline{M}_n)(M_m-\overline{M}_m)\,dx}{\sqrt{\int_{\Omega}(M_n-\overline{M}_n)^2\,dx\int_{\Omega}(M_m-\overline{M}_m)^2\,dx}}$	0	
	SAM [12], [24]	$SAM = \frac{1}{\lvert\Omega\rvert}\int_{\Omega}\arccos\left(\frac{<\boldsymbol{u},\boldsymbol{M}>}{\lvert\lvert\boldsymbol{u}\rvert\rvert_2\lvert\lvert\boldsymbol{M}\rvert\rvert_2}\right)dx$.	0	
Spatial quality metrics	FCC [8], [18]	$FCC = \frac{1}{N}\sum_{n=1}^{N}Cor(h*u_n, h*P)$, where $h = \begin{bmatrix}-1 & -1 & -1\\ -1 & 8 & -1\\ -1 & -1 & -1\end{bmatrix}$.	1	the bigger the better.
	Q^F [37]	$Q^F = \frac{\sum_{n=1}^{N}\int_{\Omega}Q^{u_nP}(x)\omega^{u_n}(x)\,dx}{\sum_{n=1}^{N}\int_{\Omega}\omega^{u_n}(x)\,dx}$, where $\omega^{u_n}(x)$ is a weight and $Q^{u_nP}(x) \in [0,1]$ is an edge information preservation value.	1	
Image quality metrics	SF [38]	$SF = \frac{1}{N}\sum_{n=1}^{N}\sqrt{\frac{1}{\lvert\Omega\rvert}\int_{\Omega}\lvert\nabla u_n\rvert^2\,dx}$.	$\sqrt{2}$	
	H [39]	$H = -\sum_{i=0}^{L-1}p_i\log_2 p_i$, where L is the gray level of the image, $p_i = n_i/n$, n_i is the probability of the number of pixels in ith gray-level, and n is the total number of pixels of the image.	∞	

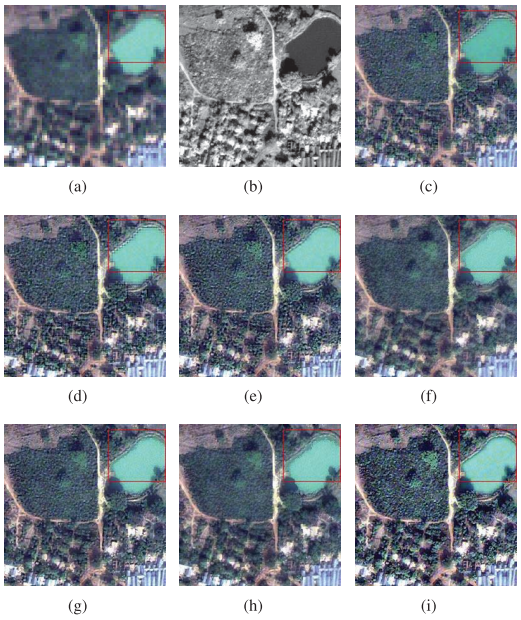

Fig. 2. Qualitative comparison: source QuickBird images (village) and the fused results using different methods. (a) The Resampled low-resolution MS image (RGB,256 × 256 pixels). (b) The High-resolution PAN images (256 × 256 pixels). (c)–(i) The Fused RGB bands by SIHS, AIHS, Wavelet, P+XS, VWP, AVWP, and proposed methods.

the above algorithms are set according to the authors' recommendations.

Figs. 2(a) and (b) and Figs. 4(a) and (b) show two QuickBird source images of one region of the Chilka Lake areas, India, acquired on February 23, 2005 12:00. Figs. 2(c)–(i) and Figs. 4(c)–(i) illustrate the results of SIHS, AIHS, Wavelet, P+XS, VWP, AVWP and proposed methods, respectively. For visual convenience, we only show the first three bands (i.e., blue, green, red bands) of each MS image.

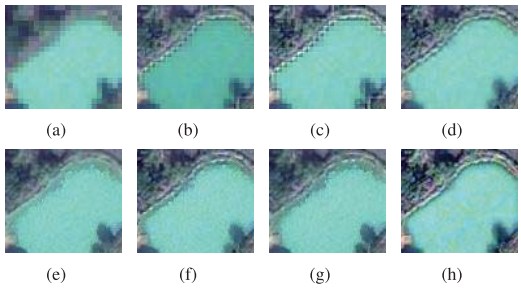

Fig. 3. Close-ups from Fig. 2. (a) The RGB band of the MS image. (b)–(h) The Fused RGB bands by SIHS, AIHS, Wavelet, P+XS, VWP, AVWP, and proposed methods, respectively.

By visually comparing the fused images, we can see that all these methods can fuse the original data effectively. However, the result images produced by other methods are relatively lack of definition and details, while the proposed results not only preserves spatial details well, but also provides high quality spectral information. To see the difference more clearly, the close-ups of an example area of Fig. 2 (in the red box) are show in Fig. 3. From Fig. 3, we can see that all images in (b)–(h) and clearer than that of (a). However, the edge of the pond is much clear in (h), while there are some staircase effects in that of (b)–(c), and blurry edges in that of (d)–(g). The similar phenomenon can also be found in the roof, roads and woods areas in Fig. 2. As another example, we can easily observe that the river in Fig. 4(i) is much clearer than that in Figs. 4(c)–(h).

Fig. 5(a) and Fig. 6(a) give two IKONOS MS source images of one mountainous area in Sichuan, China, acquired on May 15, 2008, 12:00, three days after the Wenchuan May 12 earthquake. Fig. 5(b) and Fig. 6(b) show the corresponding PAN images. The same as the QuickBird case, Figs. 5(c)–(j)

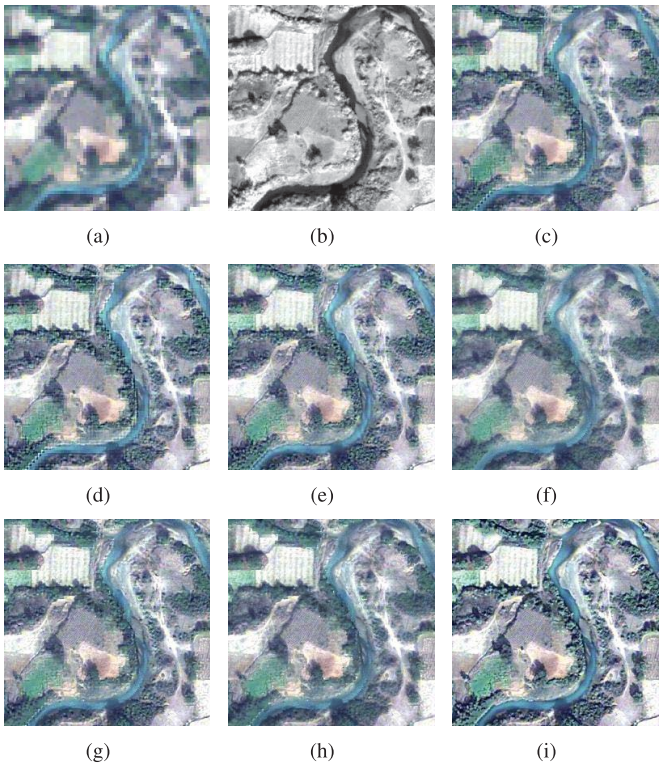

Fig. 4. Qualitative comparison: source QuickBird images(river) and the fused results using different methods. (a) The Resampled low-resolution MS image (RGB,256 × 256 pixels). (b) The High-resolution PAN images (256 × 256 pixels). (c)–(i) The Fused RGB bands by SIHS, AIHS, Wavelet, P+XS, VWP, AVWP, and proposed methods.

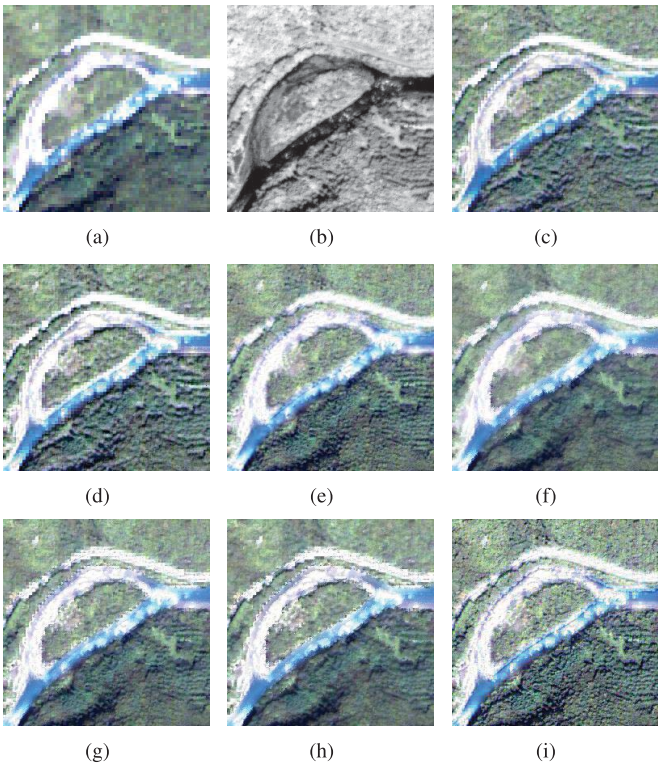

Fig. 5. Qualitative comparison: source IKONOS images (river) and the fused results using different methods. (a) The Resampled low-resolution MS image (RGB,256 × 256 pixels). (b) The High-resolution PAN images (256 × 256 pixels). (c)–(i) The Fused RGB bands by SIHS, AIHS, Wavelet, P+XS, VWP, AVWP, and proposed methods.

and Figs. 6(c)–(j) display the results of some outstanding and proposed methods, respectively. In addition, we only show the red, green, blue bands of MS images for better visual effect.

Compared with other methods, we found that our method can produce more vivid and informative results. Taking Fig. 5 as an example, the boundary of river is much clearer in (i), while in (c)–(h), they are either blurred or jagged in some degree. Besides, the sharpness of the entire image of (i) is significantly better than the others. The similar conclusion can be drawn in Fig. 6. Therefore, if we have the data that describe the same area before the Wenchuan May 12, 2008 earthquake, we can fuse it using our method and compare the fused image with that after the earthquake to get the difference more accurately. Then we can provide more accurate on-site rescue with the difference information.

Based on the above observation, we can conclude, for the visual performance, that the proposed fusion method performs better than other methods on QuickBird and IKONOS data.

C. Quantitative Analysis

In this subsection, Tables II, III, IV and V, which respectively related to Figs. 2, 4, 5 and 6, are performed to report the quantitative evaluation for seven fusion schemes including SIHS, AIHS, Wavelet, P+XS, VWP, AVWP and proposed methods. The aforementioned eight measures of four metrics categories (see Table I) are used as the quantitative criteria. Note that the best value for each quality measure are labeled in bold, and the value in the first row of each table are the reference value which related to the ideal perfect fusion result.

Observing all the tables, we can find that the proposed method is obviously better than other methods in FCC, Q^F, SF and H measures. This is justified for the following reason: As mentioned in Section V-A, FCC, Q^F are belong to the spatial quality metrics and SF, H are subject to the image quality metrics. Spatial quality metrics focus on the spatial sharpness and image quality metrics specialises in information. Since our result images are more visually clear and informative than that of the other methods obviously (have been detailed in Section V-B), to confirm our visual observations, the value of the FCC, Q^F, SF and H measures should also be higher than other methods.

In aspect of the first four measures, our method is always better than others in SAM measure, and generally dominant in RMSE, RDGES and CC measures. For example, the RDGES value of proposed method is the best one in Table II. Although the RMSE and CC values of proposed method in Table II are not the best, RMSE is only sightly larger than that of the P+XS and AVWP methods, and lower than that of all the other methods. In CC measure, the proposed method is ranked 2 in 7 methods, while SIHS method performs best. Meanwhile, we can see that the SIHS method loses all other measures, yet proposed method keeps. Thus, the proposed method is better than SIHS method. The similar results can be found in Tables III, IV and V.

TABLE II

COMPARISON OF THE PROPOSED METHOD WITH THE OUTSTANDING METHODS ON QUICKBIRD IMAGES SHOWN IN FIG. 2

	RMSE	RDGES	CC	SAM	FCC	Q^F	SF	H
Reference	0	0	0	0	1	1	$\sqrt{2}$	∞
SIHS	0.0889	5.6717	**0.0284**	2.7302	0.7787	0.4232	0.0871	7.4598
AIHS	0.1101	7.0100	0.0783	3.2710	0.8015	0.4330	0.1216	7.5807
Wavelet	0.1031	6.6192	0.1446	4.8612	0.9064	0.3431	0.1294	7.6150
P+XS	**0.0730**	4.7783	0.0886	4.1034	0.8080	0.3716	0.0820	7.4755
VWP	0.0957	6.1523	0.1279	3.2490	0.8881	0.4010	0.1194	7.5756
AVWP	0.0777	5.0528	0.0797	3.2667	0.8047	0.3753	0.0894	7.5124
Proposed	0.0878	**4.1220**	0.0718	**2.1399**	**0.9466**	**0.4436**	**0.1656**	**7.6562**

TABLE III

COMPARISON OF THE PROPOSED METHOD WITH THE OUTSTANDING METHODS ON QUICKBIRD IMAGES SHOWN IN FIG. 4

	RMSE	RDGES	CC	SAM	FCC	Q^F	SF	H
Reference	0	0	0	0	1	1	$\sqrt{2}$	∞
SIHS	0.0724	3.4543	**0.0048**	1.5391	0.7889	0.4702	0.0797	7.6942
AIHS	0.0954	4.5461	0.0379	1.9591	0.8006	0.4788	0.1084	7.7376
Wavelet	0.0863	4.1526	0.0760	3.2363	0.9080	0.3373	0.1060	7.7322
P+XS	0.0672	**3.2487**	0.0943	2.9111	0.8386	0.4421	0.0762	7.6629
VWP	0.0839	3.9923	0.0823	2.1105	0.8816	0.4064	0.1073	7.7085
AVWP	0.0754	3.5768	0.0860	2.1719	0.8208	0.4345	0.0901	7.6828
Proposed	**0.0662**	3.3019	0.0940	**1.3580**	**0.9094**	**0.4849**	**0.1394**	**7.7737**

TABLE IV

COMPARISON OF THE PROPOSED METHOD WITH THE OUTSTANDING METHODS ON IKONOS IMAGES SHOWN IN FIG. 5

	RMSE	RDGES	CC	SAM	FCC	Q^F	SF	H
Reference	0	0	0	0	1	1	$\sqrt{2}$	∞
SIHS	0.1186	5.3366	**0.0148**	2.4448	0.7338	0.4741	0.0840	7.5642
AIHS	0.1368	6.1477	0.0619	2.8057	0.7349	0.4818	0.1093	7.5540
Wavelet	0.0839	3.8188	0.0504	3.2661	0.8223	0.2179	0.1008	7.6770
P+XS	**0.0822**	3.7643	0.0475	3.3815	0.7797	0.2888	0.0857	7.6605
VWP	0.0882	4.0041	0.0556	2.4703	0.7672	0.2541	0.1111	7.6510
AVWP	0.1057	4.7610	0.0835	2.3945	0.6778	0.3047	0.1213	7.6371
Proposed	0.1002	**3.4999**	0.0678	**2.3740**	**0.8422**	**0.4828**	**0.1309**	**7.7058**

TABLE V

COMPARISON OF THE PROPOSED METHOD WITH THE OUTSTANDING METHODS ON IKONOS IMAGES SHOWN IN FIG. 6

	RMSE	RDGES	CC	SAM	FCC	Q^F	SF	H
Reference	0	0	0	0	1	1	$\sqrt{2}$	∞
SIHS	0.1776	8.3105	**0.0092**	3.4840	0.9252	0.5823	0.1652	7.7547
AIHS	0.1596	7.4860	0.0132	3.0370	0.8935	0.5432	0.1541	7.7459
Wavelet	0.1372	6.4038	0.0641	4.9070	0.9311	0.3080	0.1862	7.7695
P+XS	0.1133	4.3306	0.0318	3.6236	0.8164	0.2541	0.1170	7.7663
VWP	0.1291	5.9606	0.0380	2.4471	0.8804	0.3071	0.1733	7.7194
AVWP	0.1155	5.3099	0.0113	2.3923	0.7583	0.2716	0.1400	7.7070
Proposed	**0.1032**	**4.2022**	0.0557	**2.2965**	**0.9406**	**0.5859**	**0.2410**	**7.7785**

On the whole, the proposed method is better than other schemes, such as SIHS, AIHS, Wavelet, P+XS, VWP and AVWP methods, with respect to the related quantitative criteria, especially in spatial quality metrics and image quality metrics. This, to a large extent, has verified our qualitative analysis.

D. Computational Efficiency Analysis

To evaluate the computational efficiency, the proposed method is further compared with other variational methods, i.e., the P+XS, VWP and AVWP methods, in terms of time cost and convergence speed.

TABLE VI

TIME COMPARISON WITH OTHER VARIATIONAL METHODS (SECOND)

	P+XS	VWP	AVWP	Proposed
Fig. 2	64.0384	67.2559	23.8096	**20.7002**
Fig. 4	64.0384	63.4729	23.6926	**21.3184**
Fig. 5	63.1609	64.7209	24.5311	**19.5400**
Fig. 6	61.7764	63.8044	23.7706	**20.6315**

Firstly, with respect to time cost, we test all of the variational methods on the images in Figs. 2, 4, 5 and 6. The running time are performed in Table VI, and the best value of each figure is labeled in bold. From Table VI, we can see

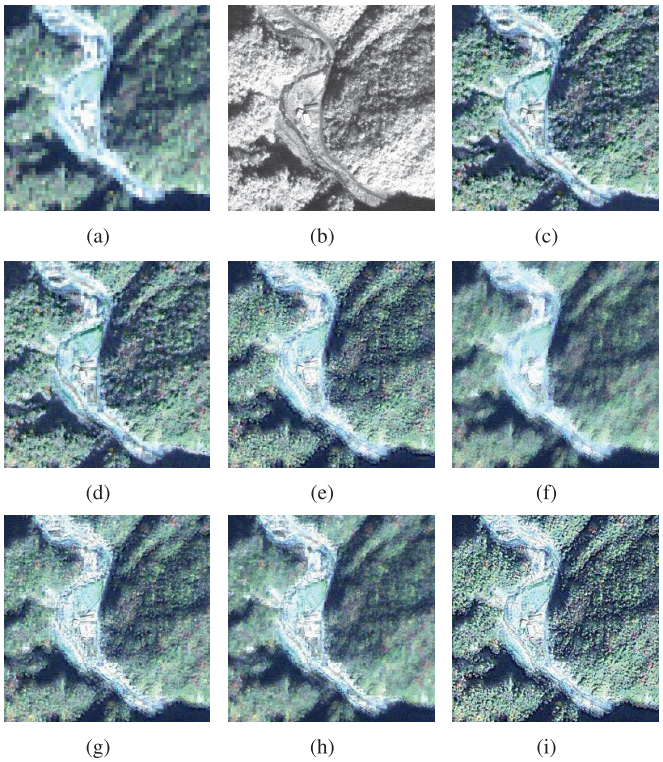

Fig. 6. Qualitative comparison: source IKONOS images(river) and the fused results using different methods. (a) The Resampled low-resolution MS image (RGB,256 × 256 pixels). (b) The High-resolution PAN images (256 × 256 pixels). (c)–(i) The Fused RGB bands by SIHS, AIHS, Wavelet, P+XS, VWP, AVWP, and proposed methods.

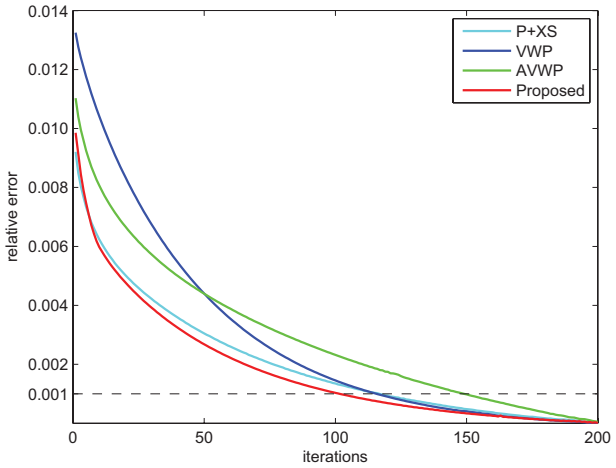

Fig. 7. Error versus iterations for the proposed method and the other variational schemes. Convergence result is for the images in Fig. 2.

that the value of the proposed method are the lowest one in all figures, which demonstrate that our method is more efficient than the other methods. The main reason is that the proposed method has no time consuming component, and we use the split Bregman iteration, which has remarkable advantages in time overhead and RAM usage, to implement our algorithm.

The convergence speed of proposed method is also presented in Fig. 7, where we have plotted the error vs. iteration line for the images in Fig. 2. As a comparison, we also draw the convergence curve for the P+XS, VWP and AVWP methods. Observing at the results, we can find the proposed method converges faster than the others. Additionally, the proposed method has reached promising results after the first 100 iterations, while to achieve the same effect, the P+XS and VWP methods need 120 iterations, and the AVWP method need 150 iterations (see the black dashed line in figure).

Therefore, we can draw a conclusion that the proposed method is much better than the other variational methods in computational efficiency aspect.

VI. Conclusion

We have introduced a variational pan-sharpening method based on three assumptions. The proposed method first performed the three assumptions, and used these assumptions to construct an energy functional. The existence of solution of energy is then discussed. For tackling functional more efficiently, we used the split Bregman algorithm to obtain the minimizing solution. In order to prove the effectiveness of the proposed method, the proposed method was applied to the Quickbird and IKONOS dataset and compared with six state-of-the-art pan-sharpening methods qualitatively and quantitatively. The results demonstrated that our method is generally better than the compared methods with respect to the related evaluations criteria. particularly, we divided the existing quantitative measures into four categories for better evaluation. Furthermore, the comparison in efficiency with other variational methods also showed the effectiveness of the proposed method. Therefore, we can conclude that the proposed method can effectively construct a high-resolution MS image which can preserve both spectral and spatial information of source images well.

Pan-sharpening is still a developing problem, and there are many open questions that should be studied. Our method is effective, but it also can be improved. For example, there are several parameters which should be chosen manually. Further research will be extended to develop some automatic methods for parameters choosing. Recently, the sparsity of the image under some certain bases have been proven efficient in many realms. We will combine our variational approach with these techniques for more excellent pan-sharpening in future.

Appendix
Proof of Theorem III

Firstly, when $\boldsymbol{u}, \boldsymbol{a}, \boldsymbol{b}$ are constants, the energy is bounded. Thus, $\inf_{(u,a,b)\in\Lambda} E \not\equiv +\infty$. Moreover, $E \geqslant 0$. Therefore, the energy (12) is well defined.

Let $\{(\boldsymbol{u}^j, \boldsymbol{a}^j, \boldsymbol{b}^j)\} \in \Lambda$ be a minimizing sequence such that $\lim_{j\to\infty} E(\boldsymbol{u}^j, \boldsymbol{a}^j, \boldsymbol{b}^j) \to \inf_{(u,a,b)\in\Lambda} E$. Thus, there exists a constant $\mathcal{M}$ such that

$$E(\boldsymbol{u}^j, \boldsymbol{a}^j, \boldsymbol{b}^j) = \int_\Omega \left| \sum_{n=1}^{N} \gamma_n D u_n^j - DP \right| + \frac{\lambda\tau}{2} \sum_{n=1}^{N} \int_\Omega (a_n^j)^2(x)dx$$

$$+\frac{\lambda}{2}\sum_{n=1}^{N}\int_\Omega\int_\Omega k(x-y)\big(a_n^j(x)u_n^j(y) +b_n^j(x)-M_n(y)\big)^2\,dy\,dx +\frac{\nu}{2}\sum_{n=1}^{N-1}\sum_{i=n+1}^{N}\int_\Omega |u_n^j-u_i^j-M_n+M_i|^2\,dx \le \mathcal{M}. \tag{28}$$

Firstly, we have

$$\frac{\lambda\tau}{2}\int_\Omega (a_n^j)^2(x)\,dx\le\mathcal{M},$$

that is, $\{a_n^j\}$ is uniformly bounded in $L^2(\Omega)$. Thus, There exists a subsequence (also denoted by $\{a_n^j\}$) and a_n^* in L^2 such that

$$a_n^j \underset{L^2(\Omega)}{\rightharpoonup} a_n^*. \tag{29}$$

By Assumption 1, $\{b_n^j\}$, where the index j corresponds to above formula, satisfies $\int_\Omega (b_n^j)^2(x)\,dx\le\mathcal{M}$, i.e., $\{b_n^j\}$ is uniformly bounded in $L^2(\Omega)$. Therefore, there exists a subsequence (also denoted by $\{b_n^j\}$) and b_n^* such that

$$b_n^j \underset{L^2(\Omega)}{\rightharpoonup} b_n^*. \tag{30}$$

Meanwhile, by formula (28), the sequence $\{u_n^j\}$, with the index j corresponds to (30), meets

$$\int_\Omega\left|\sum_{n=1}^{N}\gamma_n Du_n^j-DP\right|\le\mathcal{M}, \tag{31}$$

and

$$\int_\Omega\int_\Omega k(x-y)\big(a_n^j(x)u_n^j(y)+b_n^j(x)-M_n(y)\big)^2\,dy\,dx\le\mathcal{M}. \tag{32}$$

Thanks to Assumption 2, from (31) we have,

$$\begin{aligned}\mathcal{M}&\ge\int_\Omega|\sum_{i=1}^{N}\gamma_i Du_i^j|-\int_\Omega|DP|\\&\ge c\int_\Omega|Du_n^j|-\int_\Omega|DP|.\end{aligned}$$

So we get the boundedness of $|u_n^j|_{BV}$.

Equation (32) is equivalent to:

$$\begin{aligned}\mathcal{M}&\ge\int_\Omega\int_\Omega k(x-y)\Big((a_n^j(y)u_n^j(x))^2+2a_n^j(y)u_n^j(x)\\&\quad\times[b_n^j(y)-M_n(x)]+[b_n^j(y)-M_n(x)]^2\Big)\,dy\,dx\\&\ge\int_\Omega\int_\Omega k(x-y)(a_n^j)^2(y)\,dy\;(u_n^j)^2(x))\,dx\\&\quad+2\int_\Omega\int_\Omega k(x-y)a_n^j(y)[b_n^j(y)-M_n(x)]\,dy\;u_n^j(x)\,dx\\&\ge\int_\Omega\int_\Omega k(x-y)(a_n^j)^2(y)\,dy\;(u_n^j)^2(x))\,dx\\&\quad-2\left|\int_\Omega\int_\Omega k(x-y)a_n^j(y)[b_n^j(y)-M_n(x)]\,dy\;u_n^j(x)\,dx\right|\\&\ge\int_\Omega\int_\Omega k(x-y)(a_n^j)^2(y)\,dy\;(u_n^j)^2(x))\,dx\\&\quad-2\int_\Omega\left|\int_\Omega k(x-y)a_n^j(y)[b_n^j(y)-M_n(x)]\,dy\right.\\&\quad\left.\cdot u_n^j(x)\right|dx\\&\ge\int_\Omega\int_\Omega k(x-y)(a_n^j)^2(y)\,dy\;(u_n^j)^2(x))\,dx-2B\\&\quad\cdot|u_n^j|_{L_2(\Omega)},\end{aligned}\tag{33}$$

where

$$B=\sqrt{\int_\Omega|\int_\Omega k(x-y)a_n^j(y)[b_n^j(y)-M_n(x)]\,dy|^2\,dx}.$$

By $|a_n(x)|>\varepsilon$ in Assumption 1, we obtain

$$\begin{aligned}\int_\Omega k(x-y)[a_n^j(y)]^2\,dy&\ge\int_\Omega k(x-y)\varepsilon^2\,dy\\&=\varepsilon^2\int_\Omega k(x-y)\,dy=\varepsilon^2.\end{aligned}$$

Because the uniformly boundness of $a_n^j,\ k\in L_2(\Omega)$ and $|b_n^j|<\mathcal{M}$, we have

$$\begin{aligned}B&\le\sqrt{\int_\Omega\left(\int_\Omega|k(x-y)a_n^j(y)||b_n^j(y)-M_n(x)|\,dy\right)^2dx}\\&\le\sqrt{\int_\Omega\left(\int_\Omega|k(x-y)a_n^j(y)|\mathcal{M}\,dy\right)^2dx}\\&\le\sqrt{\int_\Omega\mathcal{M}(\|k\|_2\|a_n^j\|_2)^2\,dx}\le\mathcal{M}.\end{aligned}$$

By the above two inequalities, formula (33) can be rewritten as

$$\mathcal{M}\ge\varepsilon^2\int_\Omega(u_n^j)^2(x))\,dx-2\mathcal{M}||u_n^j||_2.$$

Hence, the L^2 norm of u_n^j is bounded by

$$||u_n^j||_2\le\frac{\mathcal{M}+\sqrt{\mathcal{M}^2+\mathcal{M}\varepsilon^2}}{\varepsilon^2}. \tag{34}$$

Then, the boundedness of $||u_n^j||_1$ is automatically obtained by

$$||u_n^j||_1\le|\Omega|^{\frac{1}{2}}||u_n^j||_2. \tag{35}$$

By the above analysis, we can conclude that $\{u_n^j\}$ is bounded in $BV(\Omega)$. Thus, there exists a subsequence (also denotes $\{u_n^j\}$) and $u_n^*\in BV(\Omega)$ such that

$$u_n^j\underset{L_1(\Omega)}{\longrightarrow}u_n^*,\quad u_n^j\underset{L_2(\Omega)}{\rightharpoonup}u_n^*\quad\text{and}\quad u_n^j\underset{BV-\mathrm{w}^*}{\rightharpoonup}u_n^*. \tag{36}$$

Therefore, up to a subsequence, there exists $\{(\boldsymbol{u}^j,\boldsymbol{a}^j,\boldsymbol{b}^j)\}$ satisfying (29), (30) and (36).

Because the weak lower semicontinuity (w.l.s.c) of L_2 norm, we have,

$$\liminf_{k\to\infty}\varepsilon\int_\Omega(a_n^j)^2(x)\,dx\ge\varepsilon\int_\Omega(a_n^*)^2(x)\,dx$$

and

$$\liminf_{k\to\infty}\frac{\nu}{2}\sum_{n=1}^{N-1}\sum_{i=n+1}^{N}\int_\Omega|u_n^j-u_i^j-M_n+M_i|^2\,dx$$

$$\geq \frac{\nu}{2}\sum_{n=1}^{N-1}\sum_{i=n+1}^{N}\int_{\Omega}|u_n^*-u_i^*-M_n+M_i|^2\,dx.$$

Thanks to Fatou lemma, we obtain that

$$\begin{aligned}
&\sum_{n=1}^{N}\int_{\Omega}\int_{\Omega}k(x-y)\big(a_n^*(x)u_n^*(y)+b_n^*(x)-M_n(y)\big)^2\,dy\,dx\\
&\quad=\sum_{n=1}^{N}\int_{\Omega}\int_{\omega_x}\frac{1}{|\omega_x|}\big(a_n^*(x)u_n^*(y)+b_n^*(x)-M_n(y)\big)^2\,dy\,dx\\
&\quad\leq\sum_{n=1}^{N}\int_{\Omega}\int_{\omega_x}\liminf_{k\to\infty}\frac{1}{|\omega_x|}\big(a_n^*(x)u_n^j(y)\\
&\qquad\qquad+b_n^*(x)-M_n(y)\big)^2\,dy\\
&\quad\leq\sum_{n=1}^{N}\int_{\Omega}\liminf_{k\to\infty}\int_{\omega_x}\frac{1}{|\omega_x|}\big(a_n^*(x)u_n^j(y)+b_n^*(x)\\
&\qquad\qquad-M_n(y)\big)^2\,dy\,dx\\
&\quad\leq\sum_{n=1}^{N}\int_{\Omega}\liminf_{k\to\infty}\left[\int_{\omega_x}\frac{1}{|\omega_x|}\big(a_n^j(x)u_n^j(y)+b_n^j(x)\right.\\
&\qquad\qquad\left.-M_n(y)\big)^2\,dy\right]\,dx\\
&\quad\leq\liminf_{k\to\infty}\sum_{n=1}^{N}\int_{\Omega}\int_{\omega_x}\frac{1}{|\omega_x|}\big(a_n^j(x)u_n^j(y)+b_n^j(x)\\
&\qquad\qquad-M_n(y)\big)^2\,dy\,dx\\
&\quad=\liminf_{k\to\infty}\sum_{n=1}^{N}\int_{\Omega}\int_{\Omega}k(x-y)\big(a_n^j(x)u_n^j(y)+b_n^j(x)\\
&\qquad\qquad-M_n(y)\big)^2\,dy\,dx.
\end{aligned}$$

Finally, for $\sum_{n=1}^{N}\gamma_n u_n^j-P\underset{BV(\Omega)}{\rightharpoonup}\sum_{n=1}^{N}\gamma_n u_n^*-P$ and the w.l.s.c of BV space,

$$\liminf_{k\to\infty}\int_{\Omega}\left|\sum_{n=1}^{N}\gamma_n Du_n^j-DP\right|\geq\int_{\Omega}\left|\sum_{n=1}^{N}\gamma_n Du_n^*-DP\right|.$$

Therefore, we can conclude that

$$\min_{(\boldsymbol{u},\boldsymbol{a},\boldsymbol{b})\in\Lambda}E(\boldsymbol{u},\boldsymbol{a},\boldsymbol{b})=\liminf_{j\to\infty}E(\boldsymbol{u}^j,\boldsymbol{a}^j,\boldsymbol{b}^j)\geq E(\boldsymbol{u}^*,\boldsymbol{a}^*,\boldsymbol{b}^*)$$

i.e., $(\boldsymbol{u}^*,\boldsymbol{a}^*,\boldsymbol{b}^*)$ is a minimum point of $E(\boldsymbol{u},\boldsymbol{a},\boldsymbol{b})$.

REFERENCES

[1] (2000). *Global Land Cover Facility* [Online]. Available: http://glcf.umiacs.umd.edu/data/ikonos/

[2] P. Chavez, S. Sides, and J. Anderson, "Comparison of three different methods to merge multiresolution and multispectral data: LANDSAT TM and SPOT panchromatic," *Photogram. Eng. Remote Sens.*, vol. 57, no. 3, pp. 295–303, 1991.

[3] K. Nikolakopoulos, "Comparison of nine fusion techniques for very high resolution data," *Photogram. Eng. Remote Sens.*, vol. 74, no. 5, pp. 647–659, 2008.

[4] T. Tu, S. Su, H. Shyn, and P. Huang, "A new look at IHS-like image fusion methods," *Inf. Fusion*, vol. 2, no. 3, pp. 177–186, 2001.

[5] M. Strait, D. Merkurjev, M. Moeller, and T. Wittman, "An adaptive IHS pan-sharpening method," *IEEE Geosci. Remote Sens. Lett.*, vol. 7, no. 4, pp. 746–750, Oct. 2010.

[6] T. Carper, T. Lillesand, and R. Kiefer, "The use of intensity-hue-saturation transformations for merging SPOT panchromatic and multispectral image data," *IEEE Geosci. Remote Sens. Lett.*, vol. 56, no. 4, pp. 459–467, Oct. 1990.

[7] Q. Du, N. Younan, R. King, and V. Shah, "On the performance evaluation of pan-sharpening techniques," *IEEE Geosci. Remote Sens. Lett.*, vol. 4, no. 4, pp. 518–522, Oct. 2007.

[8] J. Zhou, D. Civico, and J. Silander, "A wavelet transform method to merge landsat TM and SPOT panchromatic data," *Int. J. Remote Sens.*, vol. 19, no. 4, pp. 743–757, 1998.

[9] J. Nunez, X. Otazu, O. Fors, A. Prades, V. Pala, and R. Arbiol, "Multiresolution-based image fusion with additive wavelet decomposition," *IEEE Trans. Geosci. Remote Sens.*, vol. 37, no. 3, pp. 1204–1211, May 1999.

[10] C. Padwick, M. Deskevich, F. Pacifici, and S. Smallwood, "Worldview-2 pan-sharpening," in *Proc. Annu. Conf. Amer. Soc. Photogram. Remote Sens.*, Apr. 2010, pp. 1–13.

[11] C. A. Laben and B. V. Brower, "Process for enhancing the spatial resolution of multispectral imagery using pansharpening," U.S. Patent 6 011 875, Jan. 4, 2000.

[12] L. Alparone, L. Wald, J. Chanussot, and C. Thomas, "Comparison of pansharpening algorithms: Outcome of the 2006 GRS-S data-fusion contest," *IEEE Trans. Geosci. Remote Sens.*, vol. 45, no. 10, pp. 3012–3021, Oct. 2007.

[13] M. Strait, S. Rahmani, D. Markurjev, and T. Wittman, "Evaluation of pan-sharpening methods," Dept. Math., UCLA, Los Angeles, CA, USA, Tech. Rep., 2008.

[14] T. Chan, J. Shen, and L. Vese, "Variational PDE models in image processing," *Notices Amer. Math. Soc.*, vol. 50, no. 1, pp. 14–26, 2003.

[15] G. Sapiro, *Geometric Partial Differential Equations and Image Processing*. Cambridge, U.K.: Cambridge Univ. Press, 2001.

[16] G. Aubert and P. Kornprobst, *Mathematical Problems in Image Processing: Partial Differential Equations and the Calculus of Variations* (Applied Mathematical Sciences), vol. 147, 2nd ed. New York, NY, USA: Springer-Verlag, 2009.

[17] C. Ballester, V. Caselles, L. Igual, and J. Verdera, "A variational model for P+XS image fusion," *Int. J. Comput. Vis.*, vol. 69, no. 1, pp. 43–58, 2006.

[18] M. Moeller, T. Wittman, A. Bertozzi, and M. Burger, "A variational approach for sharpening high dimensional images," Ph.D. dissertation, Inst. Computational & Applied Math., Westfalische Wilhelms Universitat Munster, Münster, Germany, 2009.

[19] G. Piella, "Image fusion for enhanced visualization: A variational approach," *Int. J. Comput. Vis.*, vol. 83, no. 1, pp. 1–11, 2009.

[20] A. Levin, D. Lischinski, and Y. Weiss, "A closed form solution to natural image matting," *IEEE Trans. Pattern Anal. Mach. Intell.*, vol. 30, no. 2, pp. 228–242, Feb. 2008.

[21] K. He, J. Sun, and X. Tang, "Single image haze removal using dark channel prior," in *Proc. IEEE Conf. Comput. Vis. Pattern Recognit.*, Jun. 2009, pp. 1956–1963.

[22] K. He, J. Sun, and X. Tang, "Guided image filtering," in *Computer Vision* (Lecture Notes in Computer Science), vol. 6311. Berlin, Germany: Springer-Verlag, 2010, pp. 1–14.

[23] A. Zomet and S. Peleg, "Multi-sensor super-resolution," in *Proc. 6th IEEE Workshop Appl. Comput. Vis.*, 2002, pp. 27–31.

[24] S. Li and B. Yang, "A new pan-sharpening method using a compressed sensing technique," *IEEE Trans. Geosci. Remote Sens.*, vol. 49, no. 2, pp. 738–746, Feb. 2011.

[25] L. Rudin, S. Osher, and E. Fatemi, "Nonlinear total variation based noise removal algorithms," *Phys. D, Nonlinear Phenomena*, vol. 60, nos. 1–4, pp. 259–268, 1992.

[26] Y. Gousseau and J. Morel, "Are natural images of bounded variation?" *SIAM J. Math. Anal.*, vol. 33, no. 3, pp. 634–648, 2001.

[27] L. Ambrosio, N. Fusco, and D. Pallara, *Functions of Bounded Variation and Free Discontinuity Problems*. London, U.K.: Oxford Univ. Press, 2000.

[28] A. Chambolle, "An algorithm for total variation minimization and applications," *J. Math. Imag. Vis.*, vol. 20, no. 1, pp. 89–97, 2004.

[29] X. Tai and C. Wu, "Augmented Lagrangian method, dual methods and split Bregman iteration for ROF model," in *Proc. Scale Space Variational Methods Comput. Vis.*, 2009, pp. 502–513.

[30] T. Goldstein and S. Osher, "The split Bregman method for L1-regularized problems," *SIAM J. Imag. Sci.*, vol. 2, no. 2, pp. 323–343, 2009.

[31] *Quickbird Scene 000000185964_01_P001*, DigitalGlobe, Longmont, CO, USA, 2005.

[32] *IKONOS Scene Po_58205*, GeoEye, Dulles, VA, USA, 2008.

[33] L. Wald, T. Ranchin, and M. Mangolini, "Fusion of satellite images of different spatial resolutions: Assessing the quality of resulting images," *Photogram. Eng. Remote Sens.*, vol. 63, no. 6, pp. 691–699, 1997.
[34] T. Ranchin and L. Wald, "Fusion of high spatial and spectral resolution images: The ARSIS concept and its implementation," *Photogram. Eng. Remote Sens.*, vol. 66, no. 1, pp. 49–61, 2000.
[35] V. Vijayaraj, C. Hara, and N. Younan, "Quality analysis of pansharpened images," in *Proc. Int. Geosci. Remote Sens. Symp.*, vol. 57. 2004, pp. 85–88.
[36] I. Parcharidis and L. Tani, "Landsat TM and ERS data fusion: A statistical approach evaluation for four different methods," in *Proc. Int. Geosci. Remote Sens. Symp.*, vol. 5. 2000, pp. 2120–2122.
[37] C. Xydeas and V. Petrovic, "Objective image fusion performance measure," *Electron. Lett.*, vol. 36, no. 4, pp. 308–309, 2000.
[38] R. M. K. Sankarasubramanian, "Multi-focus image fusion based on the information level in the regions of the images," *J. Appl. Theoretical Inf. Technol.*, vol. 3, no. 1, pp. 80–85, 2007.
[39] W. Liu, J. Huang, and Y. Zhao, "Image fusion based on PCA and undecimated discrete wavelet transform," in *Proc. Int. Conf. Neural Inf. Process.*, 2006, pp. 481–488.
[40] J. John, J. Robert, S. Nikolov, D. Bull, and N. Canagarajah, "Pixel- and region-based image fusion with complex wavelets," *Inf. Fusion*, vol. 8, no. 2, pp. 119–130, 2007.
[41] S. Zheng, W. Shi, J. Liu, G. Zhu, and J. Tian, "Multisource image fusion method using support value transform," *IEEE Trans. Image Process.*, vol. 16, no. 7, pp. 1831–1839, Jul. 2007.
[42] Q. Du, O. Gungor, and J. Shan, "Performance evaluation for pansharpening techniques," in *Proc. IEEE Int. Geosci. Remote Sens. Symp.*, 2005, pp. 4264–4266.
[43] M. Choi, "A new intensity-hue-saturation fusion approach to image fusion with a tradeoff parameter," *IEEE Trans. Geosci. Remote Sens.*, vol. 44, no. 6, pp. 1672–1682, Jun. 2006.
[44] V. Petrovic, "Subjective tests for image fusion evaluation and objective metric validation," *Inf. Fusion*, vol. 8, no. 2, pp. 208–216, 2007.
[45] G. Piella and H. Heijmans, "A new quality metric for image fusion," in *Proc. IEEE Int. Conf. Image Process.*, Sep. 2003, pp. 173–176.
[46] Z. Wang, A. Sheikh, and E. Simoncelli, "Image quality assessment: From error measurement to structural similarity," *IEEE Trans. Image Process.*, vol. 13, no. 4, pp. 600–613, Apr. 2004.
[47] Z. Wang and A. Bovik, "A universal image quality index," *IEEE Signal Process. Lett.*, vol. 9, no. 3, pp. 81–84, Mar. 2002.
[48] C. Chang, "Spectral information divergence for hyperspectral image analysis," in *Proc. Int. Geosci. Remote Sens. Symp.*, vol. 1. 1999, pp. 509–511.
[49] R. King and J. Wang, "A wavelet based algorithm for pan sharpening landsat 7 imagery," in *Proc. IEEE Int. Geosci. Remote Sens. Symp.*, vol. 2. Jul. 2001, pp. 849–851.

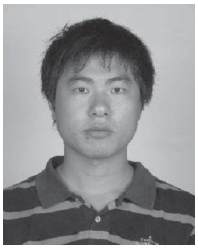

Faming Fang received the B.Sc. degree in mathematics from Shanghai Ocean University, Shanghai, China, in 2008. He is currently pursuing the Ph.D. degree with the Department of Computer Science, East China Normal University, Shanghai. His main research area is image processing using mathematical methods.

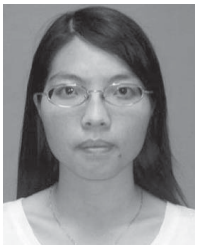

Fang Li received the M.Sc. degree from South West China Normal University, Chongqing, China, in 2004, and the Ph.D. degree from the East China Normal University, Zhongshan Bei Lu, China, in 2007, both in mathematics. She is currently an Associate Professor with the Department of Mathematics, East China Normal University. Her current research interests include anisotropic diffusion filtering, the variational methods and PDEs in image processing.

Chaomin Shen is an Associate Professor of computer science at East China Normal University (ECNU), Zhongshan Bei Lu, China. He received the Master degree from the National University of Singapore (NUS), Singapore, and the Ph.D. degree from ECNU, both in mathematics. From 1998 to 2004, he was with the Centre for Remote Imaging, Sensing and Processing (CRISP), NUS, as an Associate Scientist. His current research interests include image processing using mathematical methods and machine learning.

Guixu Zhang received the Ph.D. degree from the Institute of Modern Physics, Chinese Academy of Sciences, Lanzhou, China, in 1998. He is currently a Professor with the Department of Computer Science and Technology, East China Normal University, Shanghai, China. His current research interests include hyperspectral remote sensing, image processing, and artificial intelligence. He serves as an Associate Editor of the *Journal of Applied Remote Sensing*.